Birth of the Localized Surface Plasmon Resonance in Monolayer-Protected Gold Nanoclusters

Sami Malola,[†] Lauri Lehtovaara,[‡] Jussi Enkovaara,[§,⊥] and Hannu Häkkinen[†,‡,*]

[†]Department of Physics and [‡]Department of Chemistry, Nanoscience Center, University of Jyväskylä, FI-40014 Jyväskylä, Finland, [§]Department of Applied Physics, School of Science, Aalto University, FI-00076 Espoo, Finland, and [⊥]CSC-IT Center for Science Ltd., FI-02101 Espoo, Finland

ABSTRACT Gold nanoclusters protected by a thiolate monolayer (MPC) are widely studied for their potential applications in site-specific bioconjugate labeling, sensing, drug delivery, and molecular electronics. Several MPCs with 1−2 nm metal cores are currently known to have a well-defined molecular structure, and they serve as an important link between molecularly dispersed gold and colloidal gold to understand the size-dependent electronic and optical properties. Here, we show by using an *ab initio* method together with atomistic models for experimentally observed thiolate-stabilized gold clusters how collective electronic excitations change when the gold core of the MPC grows from 1.5 to 2.0 nm. A strong localized surface plasmon resonance (LSPR) develops at 540 nm (2.3 eV) in a cluster with a 2.0 nm metal core. The protecting molecular layer enhances the LSPR, while in a smaller cluster with 1.5 nm gold core, the plasmon-like resonance at 540 nm is confined in the metal core by the molecular layer. Our results demonstrate a threshold size for the emergence of LSPR in these systems and help to develop understanding of the effect of the molecular overlayer on plasmonic properties of MPCs enabling engineering of their properties for plasmonic applications.

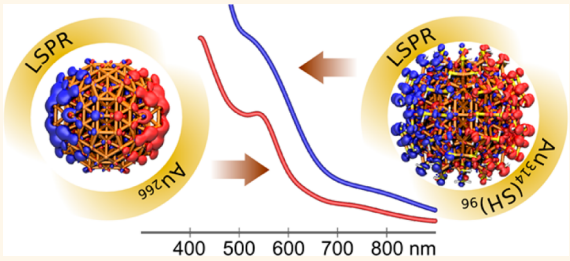

KEYWORDS: plasmon · gold · monolayer-protected cluster · optical absorption · time-dependent density functional perturbation theory · linear response

Noble metal nanoparticles (MNPs) can support localized surface plasmons resonances (LSPR) which are collective, bosonic quasiparticle excitations of the conduction electrons.[1] In the classical limit, LSPRs are electron charge density oscillations localized on the surfaces of the metal. Optical properties of large (colloidal) MNPs are dominated by excitations of LSPRs, and they can be described using the Mie theory.[2] A typical, spherical MNP has a single, strong, and broad absorption band in the UV−visible region.[3] However, LSPRs are sensitive to the size, shape, metal, and surroundings of the MNP.[4−6] The sensitivity of LSPRs increases as the particle size decreases, and below 5 nm, the classical behavior breaks down as the quantum effects step in.[7]

Plasmonic MNPs have several proposed applications, for example, in ultrasensitive chemical and biological sensing,[8,9] in medical therapeutics,[10] as nanoscale motors,[11] and antennas.[12] One of the most promising applications is single-molecule sensing *via* surface-enhanced Raman spectroscopy (SERS).[13] In SERS, the electromagnetic field induced by LSPR causes strong enhancement of the Raman signal of nearby molecules. The enhancement can be as large as 10^{12} for specific Raman modes, allowing the detection of a single molecule.[14]

Monolayer-protected clusters (MPCs) are MNPs with a definite mass and molecular composition, stabilized by a molecular layer covalently bound to the metallic core. In recent years, most the of the work has concentrated on gold MPCs stabilized by the Au−S surface bonds to organothiolates.[15−19] MPCs have an advantage of a well-defined, stable molecular structure compared to colloidal MNPs in which the variations in diameter are typically on the order of 10% and the surface metal−ligand structure is not known in the molecular scale.

Several monodisperse gold MPCs have been experimentally synthesized and structurally determined. For example, $Au_{25}(PET)_{18}^-$ (PET = phenylethylthiol),[20−22] $Au_{102}(pMBA)_{44}$

* Address correspondence to hannu.j.hakkinen@jyu.fi.

Received for review September 5, 2013 and accepted October 9, 2013.

Published online October 09, 2013
10.1021/nn4046634

(pMBA = *para*-mercaptobenzoic acid),[23] and $Au_{144}(SR)_{60}$ (SR = PET or a longer aliphatic thiol)[24−27] create a succession of nearly spherical MPCs which show a transition from a molecular to a metallic behavior. The absorption spectrum $Au_{25}(PET)_{18}^{-}$ shows a signal from clearly molecular transitions, while $Au_{102}(pMBA)_{44}$ and $Au_{144}(PET)_{60}$ have rather featureless spectra. Recent experimental reports about clusters of definite masses with slightly over 300 gold atoms[28−30] extend the list of monodisperse clusters to plasmonic gold MPCs. These clusters show a single broad peak in the spectra, which is suggested to arise from a surface plasmon. All together, the variety of known MPCs offers a great opportunity to investigate the threshold of LSPR by theoretical means.

The threshold of LSPR has been studied before using *ab initio* methods,[14] for example, using the jellium model,[31−34] or using small to medium sized silver[5,35] and gold[36,37] clusters, nanorods,[6,38] and nanowires.[39,40] The jellium model does not take into account the atomic structure, although it can be modified to take into account the local screening effects in noble metals.[33] The *ab initio* studies of gold and silver clusters indeed show that a plasmonic peak appears as the cluster size increases, but these studies do not have a direct link to any structurally known metal cluster. Moreover, LSPRs have not been theoretically analyzed in MPCs.

Here, we show computationally for the first time using an *ab initio* method together with atomistic models for true experimentally observed MPCs that the threshold diameter of the metal core for localized surface plasmon is between 1.5 and 2.0 nm in gold MPCs. We introduce a new method based on the time-dependent density functional perturbation theory (TD-DFPT) to analyze and visualize contributions of different electronic states to a spectral feature, hence, to detect for example the role of Au(5d) or Au(6sp) bands or the ligand states. We observe a distinct change in the behavior of a 540 nm (2.3 eV) excitation from the MPC of 1.5 nm core to the MPC of 2.0 nm core. In the smaller cluster, the excitation response has a collective nature but is located everywhere within the volume of the cluster, whereas in the larger cluster, the LSPR behavior is clearly seen. Moreover, we show that the 5d electrons of gold polarize creating a counter-interacting field and are therefore screening the 6sp electron oscillations of the plasmon, as would be expected according to the screened free-electron model. These findings shed light on previous experimental observations[28,29] and bring new insight into the effect of the surface metal−organic layer in LSPR phenomena.

RESULTS AND DISCUSSION

Atomic Structures. In this work, we have concentrated on two cluster systems that, from recent experiments, are known to be the borderline systems to develop plasmonic response. The smallest cluster considered is $Au_{144}(SR)_{60}$, which is known to have a faint feature in the absorption around 2.3 eV depending on the environment (solution) and the thiolate ligand used in the synthesis.[25−27,41,42] Though the precise structure of this cluster is not known at the present, our previous work[24] has established a widely used atomistic model with a 114 atom metal core and a protecting shell of 30 molecular SR-Au-SR units. This "divide and protect" geometrical motif[43] is frequently found in the structurally defined thiolate-protected gold nanoclusters as well as in thiolate monolayers on gold surfaces.[19] The Au_{114} metal core consists of a Mackay-like two-shell icosahedral geometry of 54 atoms, capped by an outer shell of 60 atoms in anti-Mackay configuration. Since in this work we will concentrate on calculating and analyzing the response of the metal core and the metal−sulfur interface to light, we have reduced the organic ligand shell to just hydrogen-passivated sulfurs; that is, in all that follows, we use SH to model SR.

We have also built an atomistic model $Au_{314}(SH)_{96}$ of the larger thiolate-protected cluster where experiments have determined a molecular mass of about 76.3−76.4 kDa with the PET ligand.[28,29] The model is an extension of the $Au_{144}(SH)_{60}$ structure described above, and it consists of a Au_{266} core with three Mackay icosahedral shells and a 120 atom anti-Mackay outer shell, protected by 48 HS-Au-SH units. This model corresponds to a mass of about 75 kDa with the PET ligand. The diameters of the gold cores are 1.5 nm for $Au_{144}(SR)_{60}$ and 2.0 nm for $Au_{314}(SH)_{96}$. We optimized the geometries of $Au_{144}(SH)_{60}$ and $Au_{314}(SH)_{96}$ clusters by using DFT (density functional theory) and calculated the optical absorption spectra by using the Casida linear reponse TDDFT (time-dependent density functional theory) formalism. For analyzing the character of the optical transitions, we developed a new method based on the time-dependent density functional perturbation theory TD-DFPT (technical details given in Methods and in Supporting Information). The same analysis was done also separately for the cores Au_{114} and Au_{266}. The structural models for Au_{114}, $Au_{144}(SH)_{60}$, Au_{266}, and $Au_{314}(SH)_{96}$ are visualized in Figure 1.

Optical Absorption. The calculated optical spectra of the model structures together with the measured experimental spectra are shown in Figure 2. A good overall agreement is found between the calculated spectrum of $Au_{144}(SH)_{60}$ and the experimental spectrum of $Au_{144}(PET)_{60}$, both being compatible also with many other experiments, such as that of $Au_{144}(PET)_{60}$ from Jin's group.[25] Rather faint but very characteristic features of $Au_{144}(SH)_{60}$ at around 540, 600, and 700 nm are visible both in the calculated spectrum as well as in the experimental data in Figure 2. The spectrum of $Au_{314}(SH)_{96}$ shows a strong plasmonic behavior at 540 nm (2.3 eV) being visible also in the measured spectrum of Dass[28] and Jin *et al.*[29] It is interesting to

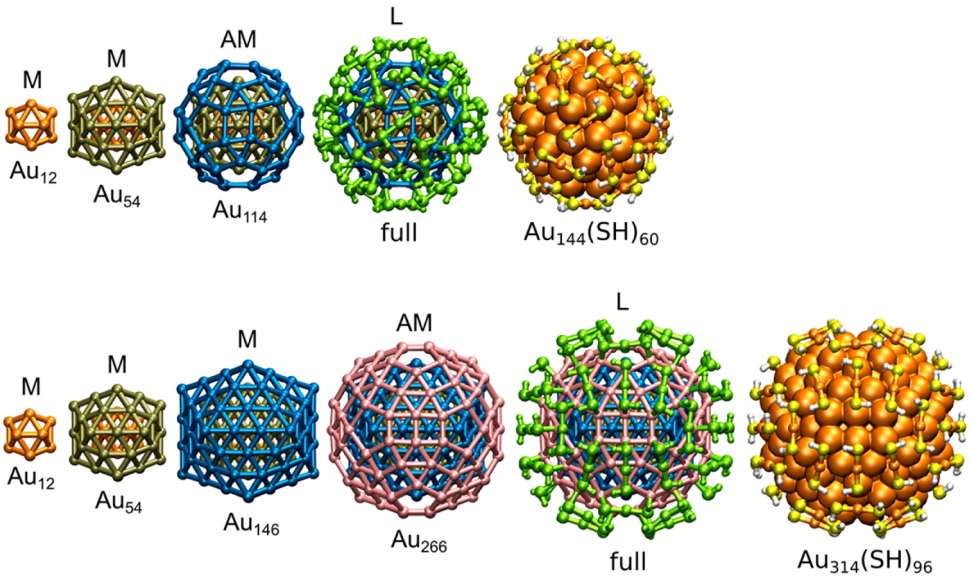

Figure 1. Atomic structures of the two studied MPCs. A layer-by-layer visualization of $Au_{144}(SH)_{60}$ (top) and $Au_{314}(SH)_{96}$ (bottom). The metal cores of both clusters are built from Mackay (M) icosahedral shells with an anti-Mackay (AM) shell at the core surface. The metal core is protected by a molecular ligand (L) layer consisting of HS-Au-SH units.

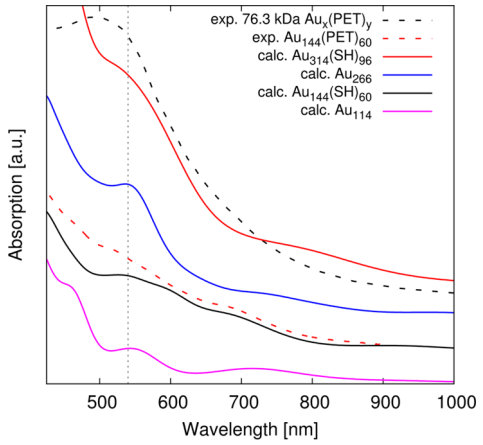

Figure 2. Calculated optical absorption spectra of the studied clusters and comparison to experiments. The spectra of Au_{114} (solid purple), $Au_{144}(SH)_{60}$ (solid black), Au_{266} (solid blue), and $Au_{314}(SH)_{96}$ (solid red) are compared to measured data for $Au_{144}(PET)_{60}$ (dashed red line, unpublished results from S. Mustalahti, P. Myllyperkiö, T. Lahtinen, K. Salorinne, S. Malola, J. Koivisto, H. Häkkinen, M. Pettersson, "Ultrafast Electronic Relaxation and Vibrational Cooling Dynamics of $Au_{144}(SC_2H_4Ph)_{60}$ Nanocluster Probed by Transient Mid-IR Spectroscopy") and to the PET-protected 76.3 kDa cluster (black dashed line, data adapted from ref 28). The computed optical transitions are broadened by 0.1 eV Gaussians. The curves for each data set have been shifted in the *y*-direction to allow for better visual comparison. We have analyzed the absorption peak at 540 nm (dotted vertical line) in all systems.

note that the Au_{266} metal core of the larger cluster already shows a distinct plasmonic band at 540 nm which is then broadened for the full particle, while the smaller core Au_{114} displays three broader features reminiscent of electron shell structure.

Excitation Profiles. Excitation profiles of the spectral features at 540 nm are shown for all systems in Figure 3 as transition contribution maps (TCM, see Methods), together with the density of occupied and empty single-particle electron states. For further analysis, it is helpful to partition the states into three categories, Au(5d), Au(6sp) band, and the states that have a dominant contribution in the ligand layer (corresponding in our model to combinations of sulfur p-orbitals and Au states at the Au−S interface, in the absence of the organic layer). In gold nanoparticles, the Au(6sp) states are delocalized over the whole particle in analogy to the free electron gas in bulk gold metal. However, the quantum confinement effects in nanoparticles create discrete energy bands with specific symmetries, and these bands are well-described by the model of "superatom".[44,45]

In the case of the protected cluster, each SH ligand withdraws one electron out from the Au(6sp) subsystem, and the effective valence numbers of Au_{114}, $Au_{144}(SH)_{60}$, Au_{266}, and $Au_{314}(SH)_{96}$ superatoms are thus 114, 84, 266, and 218, respectively. Analysis of the occupied states close to the Fermi energy of each cluster shows that analogies can be made to a spherical system in that the expected superatom state symmetries can be seen although the states with higher than D symmetry are split by the icosahedral point symmetry of the clusters (for an example of splitting the states in Au_{114}, see Supporting Information Figure S1; ref 46 shows the degeneracies and state ordering for a completely spherical system and ref 47 for a charge-perturbed particle-in-a-sphere model). The highest occupied states of Au_{114} are in the manifold 2F-1I-3P, in the region between major shell closing numbers of 92 and 138 (Figure S1), and the highest occupied states of $Au_{144}(SH)_{60}$ are known to be in the lower manifold of 2D-1H-3S.[24] Our analysis here reveals that Au_{266} shows interestingly two "supershells" of 3P-2G-1J-3D

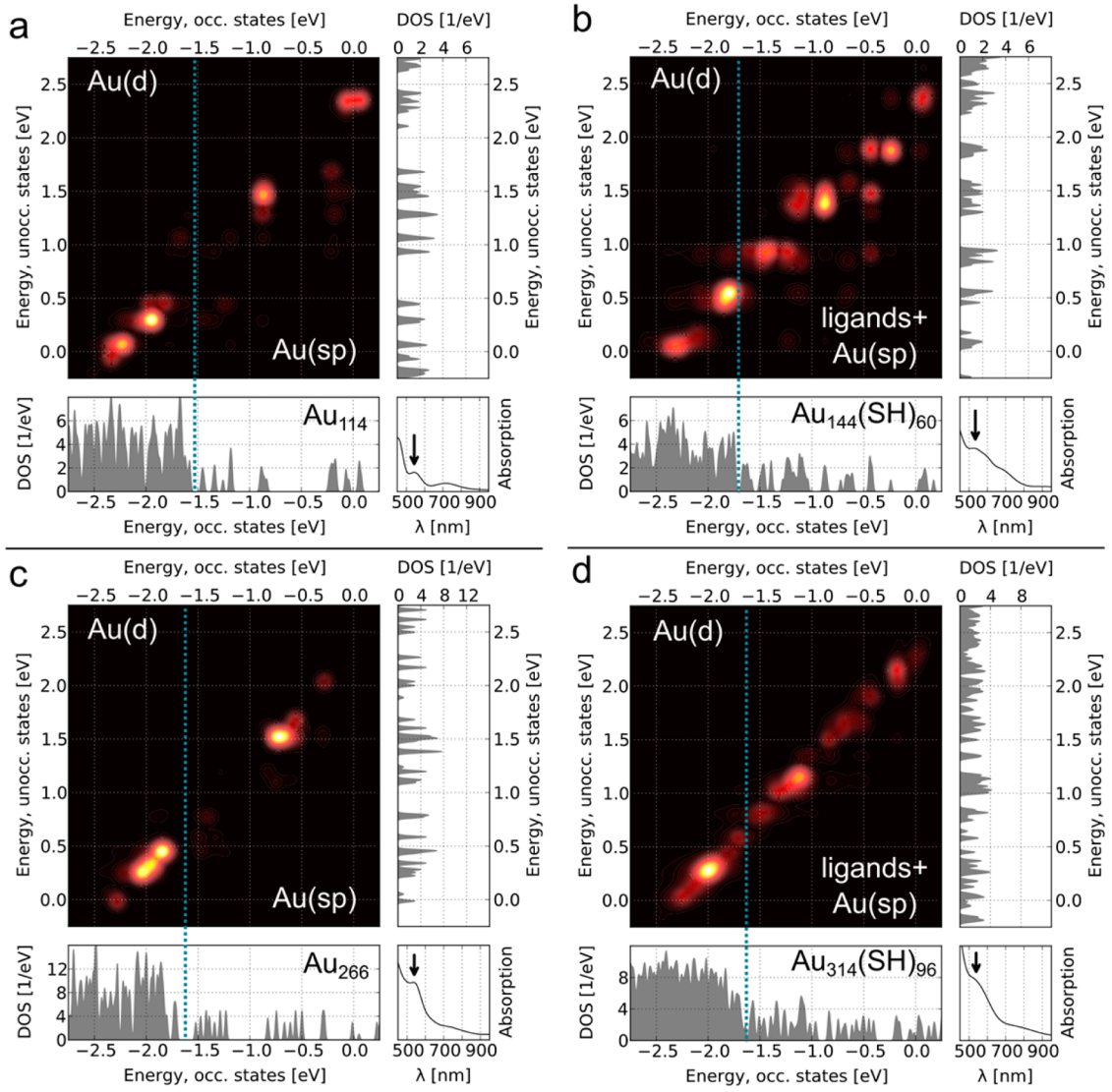

Figure 3. Transition contribution map (TCM) for the spectral features at the plasmon energy of 540 nm: (a) Au_{114}, (b) $Au_{144}(SH)_{60}$, (c) Au_{266}, and (d) $Au_{314}(SH)_{96}$. The TCM data correlate to the single-particle transitions shown in the bottom left (density of states, DOS, of the occupied KS states) and top right (unoccupied KS state) in each subfigure. The Fermi energy is at zero in the DOS plots. Arrows in the panels on bottom right show the position of the analyzed absorption peak. In the TCM visualizations, dashed blue line divides the occupied states to Au(d) band and Au(sp) band/ligand states.

(states around −1.5 eV in Figure 3c) and 4S-2H-1K (states from −0.9 to −0.6 eV in Figure 3c) manifolds. The states at the HOMO region have 3F symmetry as expected for 266 free electrons.[46] The $Au_{314}(SH)_{96}$ cluster shows these two manifolds, but shifted to higher energies. The 3P-2G-1J-3D can be found in the energy range of −1 to −0.5 eV in Figure 3d, and states are depleted from the upper manifold 4S-2H-1K that extends up to (and beyond) the Fermi energy.

The response of these free electrons to light (intraband transitions) is further affected by the local screening effects of the Au(5d) electrons (interband transitions) and the ligand (Au−S interface) states. Figure 3c shows that the plasmonic excitation at 540 nm in Au_{266} arises solely from two components: (i) a strong intraband transition from states centered around −0.75 eV to empty states around 1.5 eV, corresponding to a dipole-allowed 1K → 2J transition between the superatomic electron shells, and (ii) an interband component originating close to the edge of Au(5d) band at −2.2 to −1.8 eV. Thus, the metal core of the $Au_{314}(SH)_{96}$ cluster already has the electronic structure that is close enough to large colloidal gold particles with bulk-like inter- and intraband transitions.

Comparison of Figure 3c,d shows that while the interband component of the 540 nm excitation in $Au_{314}(SH)_{96}$ remains similar to the Au_{266} core, the intraband component has now a different contribution originating mainly from the Au−S interface states around −1.2 eV. The superatom electron transitions are still contributing but with much weaker weights. Finally, for $Au_{144}(SH)_{60}$, Figure 3b shows that the various contributions to the 540 nm excitation are spread over a wide range of single-particle energies

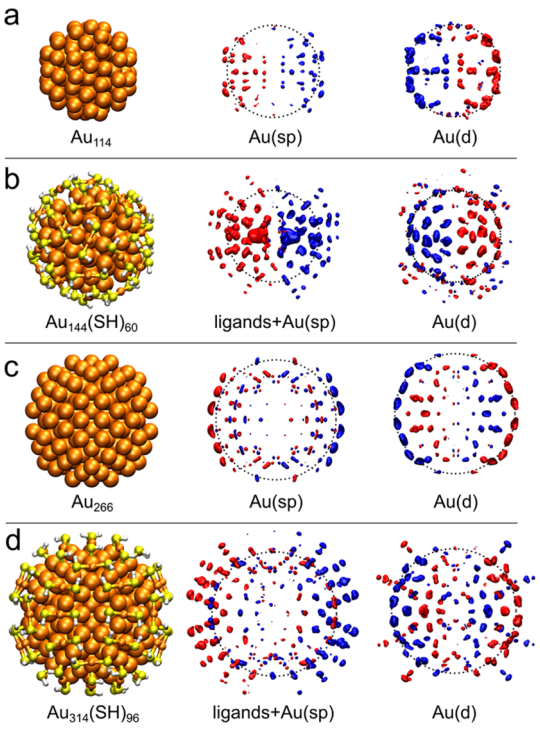

Figure 4. Structures and induced partial transition densities as calculated for the spectral features at the plasmon energy of 540 nm: (a) Au_{114}, (b) $Au_{144}(SH)_{60}$, (c) Au_{266}, and (d) $Au_{314}(SH)_{96}$. Blue and red indicate the extrema values in the density in a thin slice in real space, cutting through the middle of each cluster. The dashed circles denote the boundaries of the metal cores.

involving Au(5d) to superatom, ligand to superatom, and superatom to superatom parts. Visualized in real space, the 540 nm excitations in Figure 3a−d are distinctly different as will be discussed next.

Induced Transition Densities. The induced transition densities of 540 nm excitations in the three-cluster systems are shown in real space as projections in a thin slice through the center of the clusters in Figure 4 or as radially average profiles in Figure 5. As in the previous section, we find it useful to decompose the density in each case to contributions arising from the excitations from the Au(5d) states and from the Au(6sp) + ligand states.

A drastic qualitative difference is seen when comparing the 540 nm excitation of $Au_{144}(SH)_{60}$ (Figures 4b and 5b) to that in the larger clusters (Figures 4c,d and 5c,d). While all systems show a collective dipole-like polarization of the induced transition density at this excitation energy, the excitation is concentrated mainly inside the metal core in $Au_{144}(SH)_{60}$, whereas it is localized at the surface in the two larger clusters. The screening effect of Au(5d) electrons can be seen directly with the induced density that creates an opposing dipole moment to the Au(6sp) + ligand part in each of the systems. The maxima of the screening density of Au(5d) electrons are localized at the outermost gold layer in Au_{266}, while the maxima of the Au(6sp) transition density are just outside the metal surface (Figures 4c and 5c). When this metal core is protected by the Au-SR overlayer in $Au_{314}(SH)_{96}$, the maxima of the Au(5d) screening density are still located at the core surface, but the maxima of the Au(6sp) + ligand density are localized in the Au-SR overlayer (Figures 4d and 5d). As a conclusion, a clear qualitative change in the role of the ligand layer on the collective electronic excitation at 540 nm is seen when comparing $Au_{144}(SH)_{60}$ and $Au_{314}(SH)_{96}$. The protecting molecular layer enhances the LSPR in the bigger system, while it localizes the plasmon-like resonance in the metal core in the smaller system. To our knowledge, this surprising result has not been shown previously.

CONCLUSION

Our work provides the first detailed theoretical analysis of the nature of collective electronic excitations calculated from an *ab initio* theory for realistic atomic model structures of monolayer-protected gold nanoclusters with metal cores from 1.5 to 2 nm. We have also introduced here a novel method based on TD-DFPT to analyze and visualize contributions of different electronic states to a spectral feature, providing "transition contribution maps" that reveal the correlations between single-particle transitions within a given energy range. This information may be used for constructing simpler and numerically less demanding models for computing plasmonic response of large nanoparticles. We have shown that a gold MPC with 1.5 nm core has a collective electronic excitation at 540 nm that could be characterized as a "core-localized plasmon", while the larger clusters with 2 nm metal core support a well-developed localized surface plasmon resonance. It is interesting to note that a threshold length of 2 nm for emergence of plasmonic absorption has also been observed in calculations for finite gold nanorods.[40] These results set the brackets for the system size in which the LSPR resonance emerges for gold MPCs. Furthermore, our work stresses the importance of the ligand layer and the metal−ligand interface of gold MPCs. Since the LSPR is a surface/interface phenomenon, the excitation profile could be to some extent tuned with a suitable control of electronic properties of the ligand layer such as its π-electron density and electron affinity. Recently, it was shown that the aromatic ligand layer plays an important role in collective electronic excitations in structurally known thiol-stabilized silver nanoclusters, $Ag_{44}(SR)_{30}$.[48] It is also known in the literature that the ligand layer does have an effect on absorption around 500−600 nm in $Au_{144}(SR)_{60}$.[25−27,41,42]

Plasmonic MPCs can offer several advantages over larger, colloidal MNPs due to their modifiable ligand layer. In addition to protecting the metal core, the ligand layer offers a direct way to functionalize MPCs

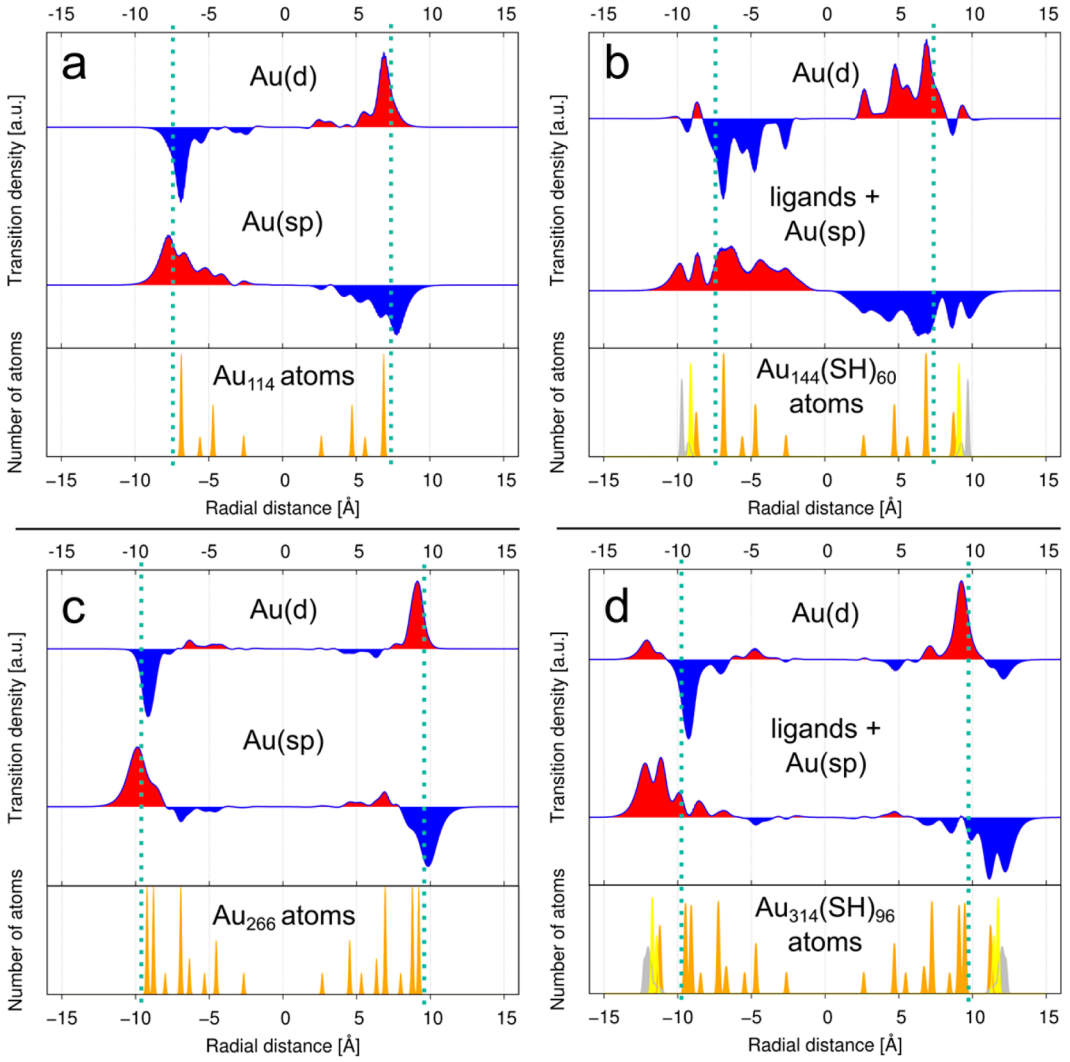

Figure 5. Radial plots of induced transition densities and atomic shell structure as calculated for the spectral features at the plasmon energy of 540 nm: (a) Au_{114}, (b) $Au_{144}(SH)_{60}$, (c) Au_{266}, and (d) $Au_{314}(SH)_{96}$. The dashed lines denote the radii of the metal cores. The atomic shells are denoted by orange for gold, yellow for sulfur, and gray for hydrogen.

for applications in diverse chemical environments. By attaching ligands that are either molecule- or site-specific, a plasmonic MPC together with SERS technique could act as an ultrasensitive and selective probe for chemical and biological sensing. Moreover, the ligand layer could be modified to bind two or more plasmonic MPCs together for plasmonic applications. It is also conceivable that the ligand layer could be engineered to include a photoactive part for catalysis and molecular machinery applications. From the theoretical point of view, it will be extremely interesting to investigate whether the plasmonic properties of small 2−5 nm MPCs can be further analyzed and understood by using an analogue to the well-established "hybridization model" for colloidal complex nanostructures.[49]

METHODS

Ground-State Electronic Structure Calculations and Geometry Optimization. We used the density functional theory (DFT) as implemented in the real-space code-package GPAW (grid-based projector-augmented wave method).[50,51] Structure optimization was performed using the local density approximation (LDA) exchange-correlation functional,[52] 0.2 Å grid spacing, and 0.05 eV/Å convergence criterion for the maximum forces acting on atoms in clusters. The LDA approximation is known to reproduce the gold−gold distances in the metal core better as compared to the higher-level functionals. The GPAW setups for gold include scalar-relativistic corrections. Optical absorption spectra were calculated for the LDA relaxed structures using Casida's formulation of the linear response time-dependent DFT[53,54] and PBE (Perdew−Burke−Ernzerhof) functional.[55]

Analysis of Optical Transitions. To analyze the transitions of the absorption spectra, we developed a method based on the time-dependent density functional perturbation theory (TD-DFPT).[56] We solve the TD-DFPT equation with a cosinoidal laser field with a selected direction of the dipole moment μ and photon frequency ω with a Lorentzian spectral broadening parameter η (see Supporting Information for details). The resulting first-order

Kohn–Sham (KS) response wave function is a weighted sum of TDDFT transitions with a chosen spectral width. As all the needed matrix elements are available from the Casida TDDFT step, the numerical solution can be efficiently done using parallel linear algebra libraries in the KS electron–hole basis. Nevertheless, TD-DFPT is not limited to the KS electron–hole basis; for example, real-space grids[56] and finite-element bases[57] can be directly used if a different method, such as time-propagation TDDFT, is used to calculate the absorption spectrum.

The response wave function can be analyzed in several ways; for example, the induced density can be obtained directly from the KS response wave function. Although it is not theoretically rigorous, further insight can be often gained by analyzing individual components of the response wave function, in the present case, the electron–hole pairs. Instead of analyzing spectral features using the traditional way (*i.e.*, transition-by-transition and electron–hole pair-by-pair), we create a "transition contribution map" (TCM), where the three axes are (1) the eigenvalue of the occupied state, "KS hole energy" ε_{occ}; (2) the eigenvalue of the unoccupied state, "KS electron energy" ε_{unocc}; and (3) the squared magnitude of the absorption coefficient $|C_{\omega,abs}|^2$. The individual transitions are broadened by Gaussians for visualization purposes (we typically use a smoothing parameter $\Delta\varepsilon = 0.1$ eV in Figure 3):

$$\mathrm{TCM}(\varepsilon_{occ}, \varepsilon_{unocc}) = \sum_{i}^{occ} \sum_{p}^{unocc} |C_{ip}^{\omega,\,abs}|^2 \times \exp\left[-\left(\frac{\varepsilon_{occ} - \varepsilon_i}{\Delta\varepsilon}\right)^2 - \left(\frac{\varepsilon_{unocc} - \varepsilon_p}{\Delta\varepsilon}\right)^2\right]$$

TCM can be combined together with other analysis methods; for example, we have successfully combined it with the superatom spherical harmonics (Y_{LM}) analysis.[44,48] Alternatively, other choices for the axes of the TCM are also possible, for example, partial density of states or a spatial projection. Here, we use TCM together with the partial density of states to divide the response wave function into two manifolds—Au(5d) manifold and superatom–ligand manifold—which are then used to construct partial induced densities for analysis.

To summarize our analysis method, we use TD-DFPT to obtain the first-order KS response wave function for a chosen spectral feature as a weighted sum of several individual TDDFT transitions. The response wave function is then used to construct TCM which allows detailed analyses of systems where spectral features arise from manifolds of transitions.

Conflict of Interest: The authors declare no competing financial interest.

Acknowledgment. We thank J. Koivisto, S. Mustalahti, and M. Pettersson for sharing unpublished data of the optical absorption of $Au_{144}(SCH_2CH_2Ph)_{60}$. H.H. thanks C.J. Ackerson and K. Knappenberger for useful discussions. This work was supported by the Academy of Finland. The computational resources were provided by CSC–the Finnish IT Center for Science in Espoo and the HRLS-GAUSS Center in Stuttgart as part of a PRACE project "Plasmonic ligand-stabilized gold nanoclusters".

Supporting Information Available: Figure S1, further details of the analysis of optical transitions based on TD-DFPT, and full ref 51. Coordinates of the clusters Au_{114}, $Au_{144}(SH)_{60}$, Au_{266}, and $Au_{314}(SH)_{96}$. This material is available free of charge *via* the Internet at http://pubs.acs.org.

REFERENCES AND NOTES

1. Kreibig, U.; Vollmer, M. *Optical Properties of Metal Clusters*; Springer: Berlin, 1995.
2. Mie, G. Beiträge zur Optik truber Medien, speziell kolloidaler Metallösungen. *Ann. Phys.* **1908**, *330*, 377.
3. Daniel, M. C.; Astruc, D. Gold Nanoparticles: Assembly, Supramolecular Chemistry, Quantum-Size-Related Properties, and Applications toward Biology, Catalysis, and Nanotechnolgy. *Chem. Rev.* **2004**, *104*, 293–346.
4. Eustis, S.; El-Sayed, M. A. Why Gold Nanoparticles Are More Precious Than Pretty Gold: Noble Metal Surface Plasmon Resonance and Its Enhancement of the Radiative and Nonradiative Properties of Nanocrystals of Different Shapes. *Chem. Soc. Rev.* **2006**, *35*, 209–217.
5. Aikens, C. M.; Li, S.; Schatz, G. C. From Discrete Electronic States to Plasmons: TDDFT Optical Absorption Properties of Ag(n) (n = 10,20,35,56,84,120) Tetrahedral Clusters. *J. Phys. Chem. C* **2008**, *112*, 11272–11279.
6. Johnson, H. E.; Aikens, C. M. Electronic Structure and TDDFT Optical Spectra of Silver Nanorods. *J. Phys. Chem. A* **2009**, *113*, 4445–4450.
7. Scholl, J. A.; Koh, A. L.; Dionne, J. A. Quantum Plasmon Resonances of Individual Metallic Nanoparticles. *Nature* **2012**, *483*, 421–427.
8. Mayer, K. M.; Hafner, J. H. Localized Surface Plasmon Resonance Sensor. *Chem. Rev.* **2011**, *111*, 3828–3857.
9. Zheng, Y. B.; Kiraly, B.; Weiss, P.; Huang, T. Molecular Plasmonics for Biology and Nanomedicine. *Nanomedicine* **2012**, *7*, 751–770.
10. Huang, X.; El-Sayed, I. H.; Qian, W.; El-Sayed, M. A. Cancer Cell Imaging and Photothermal Therapy in the Near-Infrared Region by Using Gold Nanorods. *J. Am. Chem. Soc.* **2006**, *128*, 2115–2120.
11. Liu, M.; Zentgraf, T.; Liu, Y.; Bartal, G.; Zhang, X. Light-Driven Nanoscale Plasmonic Motors. *Nat. Nanotechnol.* **2010**, *5*, 570–573.
12. Giannini, V.; Fernandez-Dominguez, A. I.; Heck, S. C.; Maier, S. A. Plasmonic Nanoantennas: Fundamentals and Their Use in Controlling the Radiative Properties of Nanoemitters. *Chem. Rev.* **2011**, *111*, 3888–3912.
13. Nie, S.; Emory, S. R. Probing Single Molecules and Single Nanoparticles by Surface-Enhanced Raman Scattering. *Science* **1997**, *275*, 1102–1106.
14. Morton, M.; Silverstein, D. W.; Jensen, L. Theoretical Studies of Plasmonics Using Electronic Structure Methods. *Chem. Rev.* **2011**, *111*, 3962–3994.
15. Templeton, A. C.; Wuelfing, M. P.; Murray, R. W. Monolayer Protected Cluster Molecules. *Acc. Chem. Res.* **2000**, *33*, 27–36.
16. Sardar, R.; Funston, A. M.; Mulvaney, P.; Murray, R. W. Gold Nanoparticles. Past, Present and Future. *Langmuir* **2009**, *25*, 13840–13851.
17. Jin, R. Quantum-Sized, Thiolate-Protected Gold Nanoclusters. *Nanoscale* **2010**, *2*, 343–362.
18. Tsukuda, T. Towards an Atomic-Level Understanding of Size-Specific Properties of Protected and Stabilized Gold Clusters. *Bull. Chem. Soc. Jpn.* **2012**, *85*, 151–168.
19. Häkkinen, H. The Gold–Sulfur Interface at the Nanoscale. *Nat. Chem.* **2012**, *4*, 443–455.
20. Heaven, M.; Dass, A.; White, P.; Holt, K.; Murray, R. W. Crystal Structure of the Gold Nanoparticle $[N(C_8H_{17})_4][Au_{25}(SCH_2CH_2Ph)_{18}]$. *J. Am. Chem. Soc.* **2008**, *130*, 3754–3755.
21. Zhu, M.; Aikens, C. M.; Hollander, F.; Schatz, G. C.; Jin, R. Correlating the Crystal Structure of a Thiol-Protected Au25 Cluster and Optical Properties. *J. Am. Chem. Soc.* **2008**, *130*, 5883–5885.
22. Zhu, M.; Eckenhoff, W. T.; Pintauer, T.; Jin, R. Conversion of Anionic $Au_{25}(SCH_2CH_2Ph)_{18}^-$ Cluster to Charge Neutral Cluster *via* Anionic Oxidation. *J. Phys. Chem. C* **2008**, *112*, 14221–14224.
23. Jadzinsky, P. D.; Calero, G.; Ackerson, C. J.; Bushnell, D.; Kornberg, R. D. Structure of a Thiol Monolayer-Protected Gold Nanoparticle at 1.1 Ångström Resolution. *Science* **2007**, *318*, 430–433.
24. Lopez-Acevedo, O.; Akola, J.; Whetten, R. L.; Grönbeck, H.; Häkkinen, H. Structure and Bonding in the Ubiquitous Icosahedral Metallic Gold Cluster $Au_{144}(SR)_{60}$. *J. Phys. Chem. C* **2009**, *113*, 5035–5038.
25. Qian, H.; Jin, R. Controlling Nanoparticles with Atomic Precision: The Case of $Au_{144}(SCH_2CH_2Ph)_{60}$. *Nano Lett.* **2009**, *9*, 4083–4087.
26. Fields-Zinna, C. A.; Sardar, R.; Beasley, C. A.; Murray, R. W. Electrospray Ionization Mass Spectrometry of Intrinsically Cationized Nanoparticles, $[Au_{144/146}(SC_{11}H_{22}N(CH_2CH_3)_3^+)_x(S(CH_2)_5CH_3)_y]^{x+}$. *J. Am. Chem. Soc.* **2009**, *131*, 16266–16271.

27. Chaki, N. K.; Negishi, Y.; Tsunoyama, H.; Shichibu, Y.; Tsukuda, T. Ubiquitous 8 and 29 kDa Gold:Alkanethiolate Cluster Compounds: Mass-Spectrometric Determination of Molecular Formulas and Structural Implications. *J. Am. Chem. Soc.* **2008**, *130*, 8608–8610.
28. Dass, A. Faradaurate Nanomolecules: A Superstable Plasmonic 76.3 kDa Cluster. *J. Am. Chem. Soc.* **2011**, *133*, 19259–19261.
29. Qian, H.; Zhu, Y.; Jin, R. Atomically Precise Gold Nanocrystal Molecules with Surface Plasmon Resonance. *Proc. Natl. Acad. Sci. U.S.A.* **2012**, *109*, 696–700.
30. Knoppe, S.; Boudon, J.; Dolamic, I.; Dass, A.; Burgi, T.; Size, T. Exclusion Chromatography for Semipreparative Scale Separation of $Au_{38}(SR)_{24}$ and $Au_{40}(SR)_{24}$ and Larger Clusters. *Anal. Chem.* **2011**, *83*, 5056–5061.
31. Puska, M. J.; Nieminen, R. M.; Manninen, M. Electronic Polarizability of Small Metal Spheres. *Phys. Rev. B* **1985**, *31*, 3486–3495.
32. Ekardt, W. E. Size-Dependent Photoabsorption and Photoemission of Small Metal Particles. *Phys. Rev. B* **1985**, *31*, 6360–6370.
33. Prodan, E.; Nordlander, P.; Halas, N. J. Electronic Structure and Optical Properties of Gold Nanoshells. *Nano Lett.* **2003**, *3*, 1411–1415.
34. Townsend, E.; Bryant, G. W. Plasmonic Properties of Metallic Nanoparticles: The Effects of Size Quantization. *Nano Lett.* **2012**, *12*, 429–434.
35. Bae, G.-T.; Aikens, C. M. Time-Dependent Density-Functional Theory Studies of Optical Properties of Ag Nanoparticles: Octahedra, Truncated Octahedra, and Icosahedra. *J. Phys. Chem. C* **2012**, *116*, 10356–10367.
36. Stener, M.; Nardelli, A.; Francesco, R. D.; Fronzoni, G. Optical Excitations of Gold Nanoparticles: A Quantum Chemical Scalar Relativistic Time-Dependent Density Functional Study. *J. Phys. Chem. C* **2007**, *111*, 11862–11871.
37. Durante, N.; Fortunelli, A.; Broyer, M.; Stener, M. Optical Properties of Au Nanoclusters from TD-DFT Calculations. *J. Phys. Chem. C* **2011**, *115*, 6277–6282.
38. Guidez, E. B.; Aikens, C. M. Diameter Dependence of the Excitation Spectra of Silver and Gold Nanorods. *J. Phys. Chem. C* **2013**, *117*, 12325–12336.
39. Bernadotte, S.; Evers, F.; Jacob, C. R. Plasmons in Molecules. *J. Phys. Chem. C* **2013**, *117*, 1863–1878.
40. Piccini, G.; Havenith, R. W. A.; Broer, R.; Stener, M. Gold Nanowires: A Time-Dependent Density Functional Assessment of Plasmonic Behavior. *J. Phys. Chem. C* **2013**, *117*, 17196–17204.
41. Ackerson, C. J.; Jadzinsky, P. D.; Sexton, J.; Bushnell, D.; Kornberg, R. D. Synthesis and Bioconjugation of 2 and 3 nm-Diameter Gold Nanoparticles. *Bioconjugate Chem.* **2010**, *21*, 214–218.
42. Negishi, Y.; Sakamoto, C.; Ohyama, T.; Tsukuda, T. Synthesis and the Origin of the Stability of Thiolate-Protected Au130 and Au187 Clusters. *J. Phys. Chem. Lett.* **2012**, *3*, 1624–1628.
43. Häkkinen, H.; Walter, M.; Grönbeck, H. Divide and Protect: Capping Gold Nanoclusters with Molecular Gold−Thiolate Rings. *J. Phys. Chem. B* **2006**, *110*, 9927–9931.
44. Walter, M.; Akola, J.; Lopez-Acevedo, O.; Jadzinsky, P. D.; Calero, G.; Ackerson, C. J.; Whetten, R. L.; Grönbeck, H.; Häkkinen, H. A Unified View of Ligand-Protected Gold Clusters as Superatom Complexes. *Proc. Natl. Acad. Sci. U.S.A.* **2008**, *105*, 9157–9162.
45. Häkkinen, H. Atomic and Electronic Structure of Gold Clusters: Understanding Flakes, Cages and Superatoms from Simple Concepts. *Chem. Soc. Rev.* **2008**, *37*, 1847–1859.
46. Martin, T. P.; Bergmann, T.; Göhlig, H.; Lange, T. Shell Structure of Clusters. *J. Phys. Chem.* **1991**, *95*, 6421–6429.
47. Guidez, E. B.; Aikens, C. M. Development of a Charge-Perturbed Particle-in-a-Sphere Model for Nanoparticle Electronic Structure. *Phys. Chem. Chem. Phys.* **2012**, *14*, 4287–4295.
48. Yang, H.; Wang, Y.; Huang, H.; Gell, L.; Lehtovaara, L.; Malola, S.; Häkkinen, H.; Zheng, N. All-Thiol Stabilized Ag_{44} and $Au_{12}Ag_{32}$ Nanoparticles with Single Crystal Structures. *Nat. Commun.* **2013**, *4*, 2422.
49. Prodan, E.; Radloff, C.; Halas, N. J.; Nordlander, P. A Hybridization Model for the Plasmon Response of Complex Nanostructures. *Science* **2003**, *302*, 419–422.
50. Mortensen, J. J.; Hansen, L. B.; Jacobsen, K. W. Real-Space Grid Implementation of the Projector Augmented Wave Method. *Phys. Rev. B* **2005**, *71*, 035109.
51. Enkovaara, J.; Rostgaard, C.; Mortensen, J. J.; Chen, J.; Dulak, M.; Ferrighi, L.; Gavnholt, J.; Glinsvad, C.; Haikola, V.; Hansen, H. A.; *et al.* Electronic Structure Calculations with GPAW: A Real-Space Implementation of the Projector Augmented-Wave Method. *J. Phys.: Condens. Matter* **2010**, *22*, 253202.
52. Perdew, J. P.; Wang, Y. Accurate and Simple Analytic Representation of the Electron-Gas Correlation-Energy. *Phys. Rev. B* **1992**, *45*, 13244–13249.
53. Casida, M.; Jamorski, C.; Bohr, F.; Guan, J.; Salahub, D. R. Theoretical and Computational Modeling of NLO and Electronic Materials. In *Recent Advances in Density Functional Methods*; ACS Press: Washington, D.C., 1996; p 145.
54. Walter, M.; Häkkinen, H.; Lehtovaara, L.; Puska, M.; Enkovaara, J.; Rostgaard, C.; Mortensen, J. J. Time-Dependent Density-Functional Theory in the Projector Augmented-Wave Method. *J. Chem. Phys.* **2008**, *128*, 244101.
55. Perdew, J. P.; Burke, K.; Ernzerhof, M. Generalized Gradient Approximation Made Simple. *Phys. Rev. Lett.* **1996**, *77*, 3865–3868.
56. Andrade, X.; Botti, S.; Marques, M. A. L.; Rubio, A. Time-Dependent Density-Functional Theory Scheme for Efficient Calculations of Dynamic (Hyper)polarizabilities. *J. Chem. Phys.* **2007**, *126*, 184106.
57. Lehtovaara, L.; Marques, M. A. L. Simple Preconditioning for Time-Dependent Density Functional Perturbation Theory. *J. Chem. Phys.* **2011**, *135*, 014103.